**Article:**
Rousseau, A., Richardson, K.H., Nandy, A. et al. (5 more authors) (2025) Exciton-diffusion enhanced energy capture in an integrated nanoscale platform. ACS Nano, 19 (15). pp. 14865-14872. ISSN 1936-0851

https://doi.org/10.1021/acsnano.4c18713

# Exciton-diffusion enhanced energy capture in an integrated nanoscale platform

Adrien Rousseau,[†,¶] Katherine Richardson,[‡,¶] Atanu Nandy,[†] Cvetelin Vasilev,[‡] Madeline P. Hoffmann,[†] C. Neil Hunter,[‡] Matthew P. Johnson,[*,‡] and Gabriela S. Schlau-Cohen[*,†]

†*Department of Chemistry, Massachusetts Institute of Technology, Cambridge, MA 02139 USA*

‡*Plants, Photosynthesis and Soil, School of Biosciences, University of Sheffield, Firth Court, Western Bank, Sheffield, UK*

¶*These authors contributed equally.*

E-mail: matt.johnson@sheffield.ac.uk; gssc@mit.edu

**Abstract**

Harnessing solar energy through biologically-inspired nanoscale platforms presents a promising route for sustainable energy conversion. Biohybrid systems take advantage of the design and performance of natural systems while also enabling optimized organization of the protein components. Until now, such systems have usually been made from components of the same species, limiting the range of properties and interactions that can be generated. Here, we introduce a nanoscale platform of biomolecular films containing cross-species antenna/reaction center proteins. We demonstrated long-range exciton diffusion of ∼200 nm through the antenna light-harvesting complex II (LHCII) from green plants and quantified the underlying diffusivity at $3 \times 10^{-2}\,\mu m^2 ns^{-1}$ using complementary simulations. The LHCII micro-pattern also induced directional exciton

diffusion as a crucial mechanism for enhanced energy capture, yielding a ∼30% energy transfer efficiency to the reaction center - light-harvesting complex 1 (RC-LH1) complex from purple bacteria. This platform provides a proof-of-concept for an operation-ready, hybrid energy harvesting system capable of spanning the entire visible spectrum. These results pave the way for integrating diverse photosynthetic proteins into biofilm platforms, offering new potential for solar energy capture and conversion.

## Keywords

Artificial photosynthesis, Biophotovoltaics, Protein networks, Energy transfer, Exciton diffusion, Renewable energy technologies

## Introduction

Nanoscale platforms inspired by biological systems present a promising avenue for achieving efficient solar energy conversion. In Nature, antenna and reaction center proteins perform energy capture and conversion with high quantum efficiency.[1–4] By leveraging the performance of these protein components, biohybrid systems can potentially organize these components to perform solar energy conversions with efficiencies that match —or even exceed —biological systems.[5–13] A key factor in enhancing energy capture within such nanoscale platforms is diffusion of the electronic excited states, or excitons, a process well-documented in organic photovoltaics but largely unexplored within biomolecular films.[14–19] In organic systems, exciton diffusion is known to significantly improve overall device efficiency by enhancing the capture of the photo-generated excitons within the active layer.[15–18] Despite the clear importance of this mechanism in synthetic systems, the properties of exciton diffusion and their optimization in biohybrid nanoscale platforms remain poorly understood. Achieving such an understanding could drive significant advancements in the design of these platforms.

Integration of photosynthetic proteins from different organisms into biohybrid nanoscale platforms offers an intriguing solution to overcoming the spectral limitations of individual photosystems.[20]For instance, light-harvesting proteins from higher plants, such as LHCII, excel at capturing visible light, while proteins from bacteria, such as the reaction center - light-harvesting complex 1 (RC-LH1), are tuned to absorb near-infrared light.[21–23] This is of particular interest given the significant efforts devoted to enhancing silicon-based solar cell technologies to capture far-red light from the solar spectrum.[24] Combining these proteins into a single platform could enable solar energy capture across the entire visible spectrum.[20]Achieving efficient energy transfer between such disparate systems is challenging, however, owing to minimal spectral overlap and the distinct evolution of their light-harvesting machinery.[23]

In this work, we demonstrate the first evidence of long-range exciton diffusion and sensitization in a hybrid nanoscale platform composed of LHCII from higher plants and RC-LH1 from purple bacteria, building on the pioneering work of *Liu et al.*[25] Our findings reveal energy transfer between these proteins, with an efficiency of approximately 30%. We measured exciton diffusion lengths of about 200 nm in the LHCII biomolecular film and determined a diffusivity of $3 \times 10^{-2}\,\mu m^2 ns^{-1}$ through complementary simulations. These results suggest that directional exciton diffusion could be leveraged to improve energy capture in analogous biohybrid systems. This study presents a blueprint for the architecture of biohybrid nanoscale platforms, thereby providing a pathway to the development of fully operational, broad-spectrum biophotovoltaic systems.

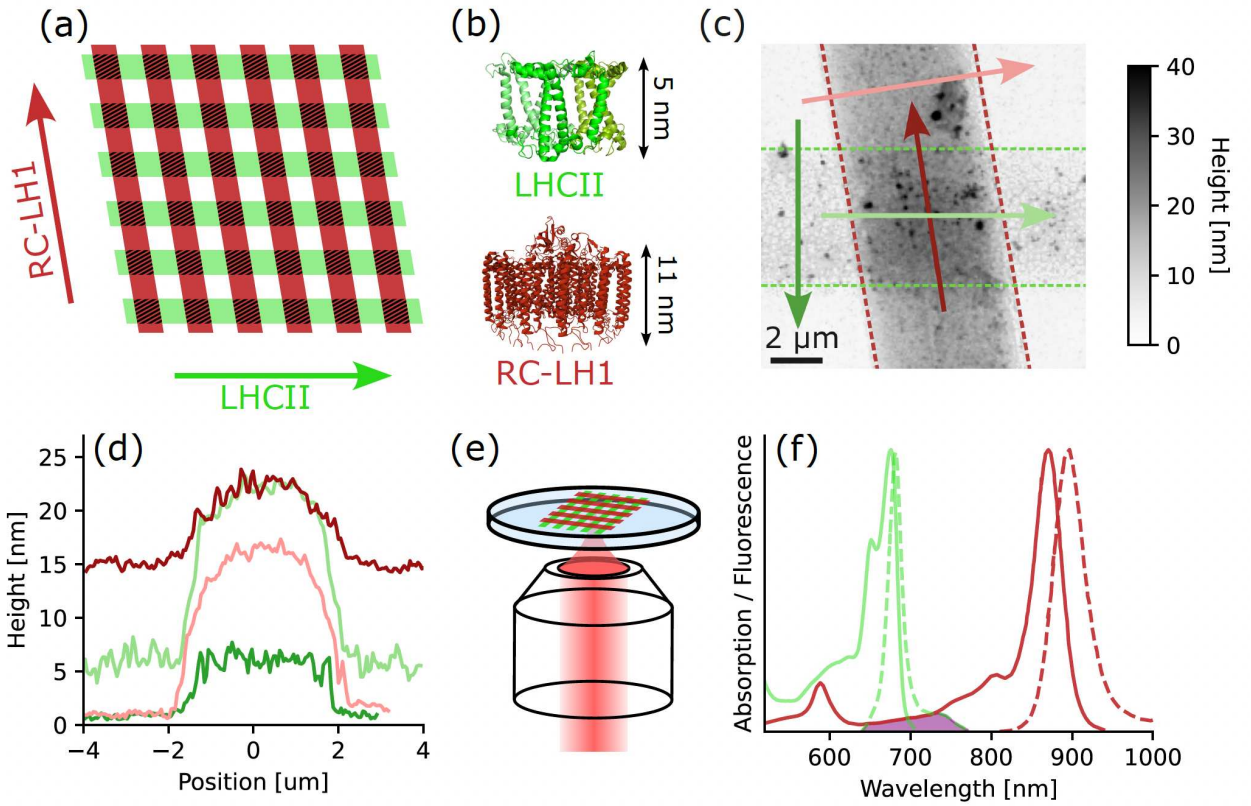


Figure 1: (a) Schematic representation of the LHCII/RC-LH1 protein network (b) and 3D representation of LHCII and RC-LH1 proteins, where the pigments are omitted, with their corresponding height. (c) AFM topography of the LHCII/RC-LH1 protein network, where the color code gives the height. (d) AFM profiles along the paths represented on panel (c). (e) Microscope configuration where the LHCII/RC-LH1 protein network on a glass coverslip sits on top of the microscope objective. (f) Absorption and fluorescence (solid/dashed lines) spectra of LHCII (green) and RC-LH1 (red).[26–29] The purple shaded area represents the overlap between LHCII fluorescence and RC-LH1 absorption, where the energy transfer can occur. The excitation wavelength is 630 nm.

# Results

## Nanoscale platform fabrication and characterization

We employed a two-step micro-contact printing method, as developed by *Huang et al.*,[10] to fabricate a two-dimensional grid of cross-patterned protein networks of LHCII from spinach and RC-LH1 from *Rhodobacter (Rba.) sphaeroides* on poly-L-lysine coated glass coverslips. The resulting linear patterns of LHCII and RC-LH1, shown in green and red in Figure 1a, are 5 µm wide, separated by 5 µm, and oriented approximately orthogonally. The regions of overlap between LHCII and RC-LH1 are indicated by the hashed areas in Figure 1a.

The sample topography was measured using atomic force microscopy (AFM) and is presented in Figure 1b-d. The AFM image revealed a cross-pattern (Figure 1c) with the vertical (horizontal) strip delineated by the red (green) dashed lines exhibiting approximate thicknesses of 11 nm (5 nm) corresponding to the heights of RC-LH1 (LHCII) as illustrated in Figure 1b. The height profiles extracted along the path of delineated strips are shown in panel d with analysis reported in Table S0. In the RC-LH1 cross-section, the height was at the expected 11 nm at the edges whereas it increased up to 15 nm in the center, which may be attributed to different protein orientations induced by higher density in this region. The nearly constant height of the LHCII cross-section can be explained by the smaller and/or more symmetric protein structure as the deposition method does not allow any control over protein orientation on the surface. The height in the overlap region ranged from 16 to 21 nm in good agreement with the expected values for the two proteins overlapping. The agreement between the heights and the dimensions of the proteins indicates that LHCII and RC-LH1 are deposited as monolayers in the nanoscale platform, forming a bilayer in the overlap region. Analysis of the root-mean-square displacement of the height profiles showed minimal variation of ∼1 to 2 nm (Table S0), indicating densely packed and homogeneous protein layers.

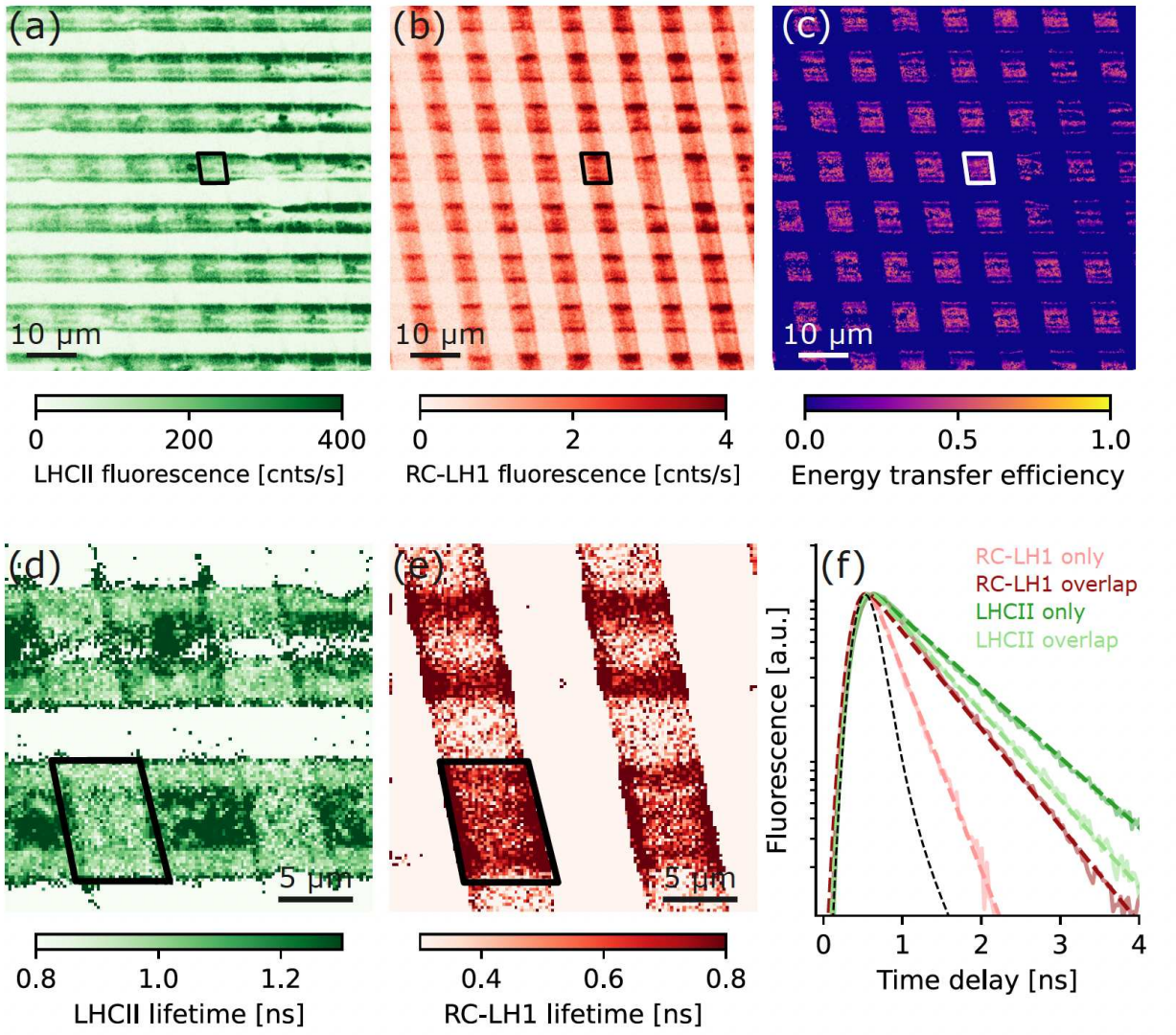


Figure 2: Fluorescence intensity maps (a, b) and FLIMs (d, e) of LHCII and RC-LH1 recorded over the same area of the LHCII/RC-LH1 network. (c) Energy transfer efficiency map derived from the fluorescence intensity of LHCII and RC-LH1 in panel (a). The parallelograms in panels a-e highlight a region of overlap. (f) Fluorescence decay curves for LHCII (lighter/darker green solid lines) and RC-LH1 (darker/lighter red solid lines) measured inside/outside the overlap regions. The dashed black line depicts the instrument response function (IRF).

## Evidence of energy transfer in LHCII/RC-LH1 network

Fluorescence intensity maps of LHCII (∼700 nm) and RC-LH1 (∼900 nm) (Figure 1f) were recorded simultaneously for the LHCII/RC-LH1 protein network as shown in Figure 2a and b. Each 100x100 µm$^2$ map displayed nearly orthogonal 5 µm wide periodic lines corresponding to the LHCII (green) and RC-LH1 (red) linear patterns, reflecting the architecture of the nanoscale platform. The excitation wavelength (630 nm) mainly excites LHCII, although 10% of the excitation is absorbed by RC-LH1. Thus, there is a weak signal in the RC-LH1 only regions of the map in Figure 2b. A weak signal attributed to fluorescence leakage from LHCII into the RC-LH1 channel is also observed in the LHCII only regions in Figure 2b. LHCII fluorescence is approximately 100 times stronger (∼200 counts/s) than that of RC-LH1 (∼2 counts/s) because there is minimal direct excitation of RC-LH1 due to its lower absorbance of RC-LH1 at 630 nm (Figure 1f). Intensity changes along both patterns, as seen in Figure 2a and b, coincide with the overlapping regions. In these regions, LHCII fluorescence is quenched by nearly 40%, while RC-LH1 fluorescence increases by a factor of 2, thus providing direct evidence of excitation energy transfer (EET) from LHCII to RC-LH1. An enhanced fluorescence signal was observed at the edges of the LHCII and RC-LH1 patterns. The AFM images (Figure 1d) show an even distribution of both LHCII and RC-LH1 across each pattern. At the edges, the number of neighboring complexes is halved, which would decrease the well-established aggregation-induced quenching in these complexes.[30–34] Consistent with this picture, the lifetime increased in these regions. Additionally, the diffusion path is effectively halved, reducing the possibility of singlet-triplet quenching. Our interpretation is further supported by significantly higher fluorescence intensities and increased LH1-RC lifetime (top strip in Figure 2d,e) for broken strips, where confinement is further amplified. The energy transfer efficiency ($E$) across the map, shown in Figure 2c, was estimated using

$$E = 1 - \frac{I'_D}{I_D} \tag{1}$$

where $I'_D$ is the LHCII intensity at each point, and $I_D \sim 250$ counts, the average LHCII fluorescence intensity outside the overlap regions. The estimated E reaches values as high as 64%, with an average of $\sim 30 \pm 10\%$ on the overlap regions, and no EET outside the overlaps.

Fluorescence lifetime imaging (FLIM) was also conducted on the same LHCII/RC-LH1 protein network, and the results are shown in Figure 2d and e for LHCII ($\sim$700 nm) and RC-LH1 ($\sim$900 nm), respectively. The color code represents the fitted lifetime at each point on the maps, corresponding to the color bars. Fluorescence decay curves for LHCII (lighter/darker green) and RC-LH1 (darker/lighter red), measured inside/outside the overlap regions, are presented in Figure 2f. As expected, a change in the fluorescence lifetime of both LHCII and RC-LH1 was observed in the overlap regions. The fluorescence lifetime of LHCII outside the overlap regions, $\tau_D \sim 1.3 \pm 0.2$ ns, dropped to $\tau'_D \sim 1.0 \pm 0.2$ ns in the overlap regions due to quenching by RC-LH1. Conversely, the fluorescence lifetime of RC-LH1 outside the overlap regions, $\tau_A \sim 0.4 \pm 0.1$ ns, increased significantly to $\tau'_A = 0.8 \pm 0.1$ ns. This increase is attributed to the RC-LH1 fluorescence in the overlap regions arising from EET from LHCII, which continues for the lifetime of LHCII. The energy transfer efficiency, estimated from the LHCII fluorescence lifetime using $E = 1 - \frac{\tau'_D}{\tau_D}$, is approximately $35 \pm 10\%$, which falls within error of the value extracted from fluorescence intensity.

The $\sim$30% energy transfer efficiency observed in our LHCII/RC-LH1 protein network is comparable to the $E \sim 40\%$ efficiency reported by *Huang et al.* for LH2/RC-LH1 protein networks, where both proteins were purified from the same species.[10] Energy transfer depends on both the donor-acceptor separation, with a $1/r^6$ dependence on their distance, and the spectral properties of the donor and acceptor, with a linear dependence on their overlap.[35,36] While the distance is determined by the network geometry and protein structures, spectral overlap emerges as an additional parameter behind the energy transfer efficiency through such networks. In LH2/RC-LH1 networks, the efficiency was largely attributed to

the significant spectral overlap between LH2 and LH1, a consequence of their co-evolution to optimize energy transfer.[10] In contrast, the ∼30% efficiency in the LHCII/RC-LH1 network is particularly striking given the minimal spectral overlap between LHCII and RC-LH1 (see Figure 1f). The cross-species pairing of LHCII and RC-LH1, which lacks the evolutionary fine-tuning of native systems, makes this observed efficiency a key milestone for cross-species biohybrid platforms. A plausible explanation for this high efficiency is long-range exciton diffusion within the LHCII layer, which increases the number of photogenerated excitons that reach RC-LH1 to enhance its energy capture.

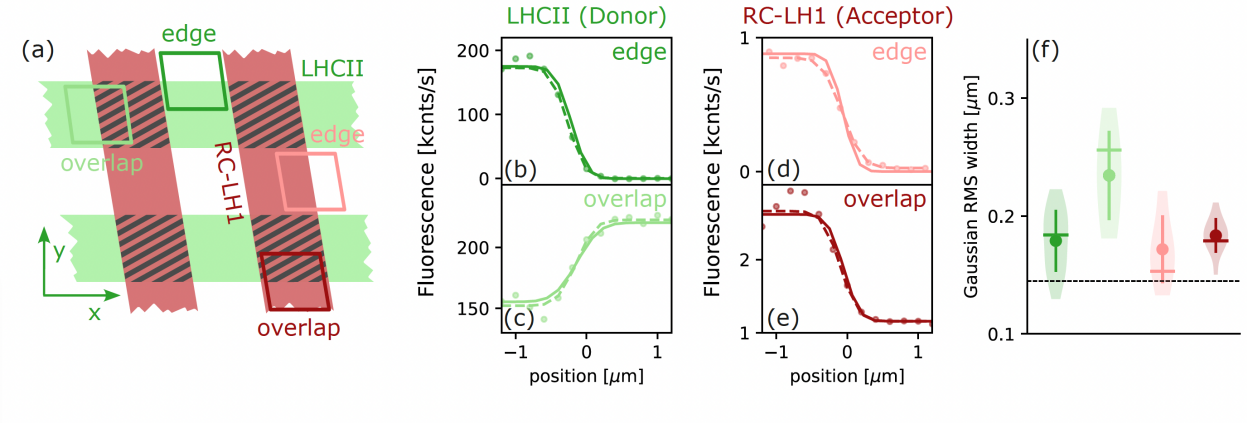


Figure 3: (a) Diagram of the path corresponding to the different extracted profiles in panels b to e. Typical fluorescence intensity profiles of LHCII (b, c) and RC-LH1 (d, e) across pattern edges (a, c) and overlap regions (b, d) extracted from Figure 2. Measured profiles are shown as data points, with their fits in dashed lines. Simulated profiles are shown by the solid lines. (f) Root-mean-squared (RMS) widths from intensity profiles are shown in violin plots, with mean values and standard deviations depicted by points and error bars. Horizontal lines show widths extracted from the simulation.

## Long-range exciton diffusion

To characterize the exciton diffusion, intensity profiles for LHCII and RC-LH1 were extracted from Figure 2a and b. Representative profiles are shown in Figure 3 for LHCII (b, c) and RC-LH1 (d, e), spanning both the pattern edges and the overlap regions. The edge profiles (b, d), obtained outside the overlap regions where no energy transfer occurs, served as

benchmarks for our spatial analysis by providing the spatial resolution for each channel. These profiles exhibit a characteristic error function shape, arising from the convolution of a step function—representing the pattern or overlap region edges—with a Gaussian function that describes the local exciton population, defined as:[37]

$$I(x) = A \int_{-\infty}^{x} e^{-\frac{\tau^2}{2\sigma^2}} d\tau + B \tag{2}$$

where $A$ and $B$ denote the amplitude and baseline of the intensity profile, respectively, and $\sigma$ represents the root-mean-square (RMS) width of the Gaussian distribution. The fits obtained for each profile are shown as dashed lines in Figure 3b-e. RMS widths extracted for each fit over 10-15 edges are presented as violin plots in Figure 3f, with the mean values and standard deviations depicted by points and error bars. The extracted widths of the edge profiles closely align with the theoretical diffraction limit of our excitation spot, approximately 144 nm, as indicated by the dashed horizontal line.

The overlap profiles Figure 3c and e, obtained for the regions where energy transfer occurs, were analyzed to extract the spatial evolution of the excitons. The widths obtained from the fits of the RC-LH1 overlap profiles were similar to the widths from the RC-LH1 edge profiles. Notably, widths obtained from the fits of the LHCII overlap profiles were broader than the edge profiles, with an average RMS width of 250 nm, nearly twice the spatial resolution. The sharp edges of less than 50 nm in the AFM profiles in Figure 1d indicate that the observed broadening arises from exciton dynamics. Specifically, these findings suggest that the exciton population in LHCII decreases gradually upon approaching the overlap regions, broadening the Gaussian width in the intensity profile. This gradual decrease in fluorescence intensity can be attributed to long-range exciton diffusion in LHCII, where excitons generated in the LHCII network diffused toward RC-LH1 and were quenched via energy transfer and subsequent charge separation.

To explore the underlying dynamics, spatiotemporal simulations of exciton diffusion were

performed using general equations for exciton dynamics in molecular films, with LHCII as the donor and RC-LH1 as the acceptor:[15]

$$\frac{dn_D}{dt} = G(t) + D_x\frac{\partial^2 n_D}{\partial x^2} + D_y\frac{\partial^2 n_D}{\partial y^2} - (k_D + k_{ET})n_D \tag{3}$$

$$\frac{dn_A}{dt} = k_{ET}n_D - k_A n_A \tag{4}$$

where $n_D$ and $n_A$ represent the exciton densities of the donor and acceptor, respectively, and $k_D$ and $k_A$ are their radiative rates. $G(t)$ is the exciton generation term for the donor, $D_x$ and $D_y$ are the exciton diffusion coefficients, and $k_{ET}$ is the energy transfer rate from donor to acceptor. We make a nearest-neighbor approximation as next-nearest-neighbors give rates $\sim 10^5$ lower due to the steep distance dependence and dimensions of LHCII. Numerical simulations based on this spatiotemporal model were performed using the finite-difference time-domain (FDTD) method on a $63 \times 63$ matrix, with spatial steps of 160 nm and time steps of 0.1 ns. The values of $k_D$, $k_A$, and $k_{ET}$ were derived from the FLIM measurements of the previous section, while $D_x$ and $D_y$ were treated as free parameters. The parameters yielding the best match with our experimental data are listed in Table 1, and the results of the simulation are displayed in Figure SS1. The simulated intensity profiles, extracted from the simulation, are shown as solid lines in Figure 3b-e.

Table 1: Parameters used for the exciton diffusion simulation.

| Parameters | $L_D$ | $D_x$ ($D_y = 0.4D_x$) | $k_D$ | $k_A$ | $k_{ET}$ |
|---|---|---|---|---|---|
| Values | 200 nm | $3 \times 10^{-2}$ µm$^2$ns$^{-1}$ | 0.83 ns$^{-1}$ | 2.5 ns$^{-1}$ | 0.25 ns$^{-1}$ |

The best match with our experimental data occurred when $D_x = 0.4D_y$. Similar agreement with experimental data could not be achieved using isotropic exciton diffusion ($D_x = D_y$). As illustrated in Figure SS3d, our findings show directional exciton diffusion within LHCII along the linear pattern ($x$). This behavior can be attributed to excitonic confinement

along the transverse ($y$) direction, resulting in directional energy transport, as reported previously in LH2 arrays.[38] Based on the diffusion coefficient, we estimated an exciton diffusion length of approximately 200 nm, consistent with the RMS widths measured at the overlap region edges for LHCII. Analysis of our simulations shows a timescale of approximately 9 ps for a particle to travel 7 nm, which is the diameter of LHCII. Previous research, specifically structure-based theoretical calculations, found that LHCII-to-LHCII energy transfer can occur as quickly as 5 ps.[39] This aligns with our observed timescale of around 9 ps for directional motion. The heterogeneous LHCII orientations in the nanoscale platform remove the alignment intrinsic to native membranes. However, the transition dipole moments of LHCII are near-isotropic,[40,41] meaning that minimal orientational effects are expected and consistent with the agreement between our results and previous structure-based calculations.[39] Notably, 200 nm is approximately four-fold the diffusion length required in plant membranes, thereby ensuring near unity efficiencies.[42–44]

Lifetime profiles of LHCII and RC-LH1 were also studied across the overlap regions from FLIMs in Figure 2d and e, and are shown in Figure SS3. Similar widths were obtained for LHCII and RC-LH1, with LHCII widths 1.5 times larger than RC-LH1 with a mean value centered around 230 nm. The lifetime profiles obtained from the simulation correctly reproduced our data, where the extracted widths showed good agreement with the experimental values.

The observed diffusion length of 250 nm in the LHCII is longer than the diffusion length of approximately 50 nm in the PSII supercomplex in native membranes. In the supercomplex, the diffusivity is estimated to be $\sim 5 \times 10^{-4}\,\mu m^2 ns^{-1}$,[42,45] two orders of magnitude below the value in our nanoscale platform. The lower diffusivity in the native membranes may be due to differences in the organization of the protein network. In the nanoscale platform, the AFM images show a dense and closely packed network of LHCII, whereas the thylakoid has

only ∼80% protein occupancy. In single-protein-width LH2 arrays,[38] the diffusion length for LH2 is longer (up to ∼700 nm) with a diffusivity of ∼0.3 $\mu m^2 ns^{-1}$,[38] reflecting an order of magnitude greater diffusivity for LH2 as compared to LHCII. The shorter diffusion length in our system is also due to the reduced confinement for the LHCII pattern, in which the width consists of approximately a thousand proteins. In both the LH2 arrays and our study, the findings highlight the potential of protein micro-patterns to actively guide energy along specific directions even with moderate confinement.

To validate our findings, we performed a power-dependent study of the fluorescence intensity and lifetime in the LHCII/RC-LH1 network as shown in Figure SS4. Detailed results are provided in the Supplementary Information. We observed a sub-linear power dependence above an excitation fluence of 100 $\mu J cm^{-2}$, accompanied by a reduction in fluorescence lifetime, indicative of exciton-exciton annihilation. Previous work by *Gruber et al.* showed that singlet-triplet annihilation predominates in LHCII trimers.[46] Using a similar model, adapted for our system and accounting for RC-LH1, we successfully reproduced our experimental data. From our model, we extract a singlet-triplet annihilation rate ($\gamma_{st}$) for LHCII of 0.7 $ns^{-1}$, corresponding to a singlet exciton diffusion length of approximately 200 nm, consistent with our spatial analysis. The annihilation time ($1/\gamma_{st}$ ∼1.4 ns) is similar to the singlet exciton lifetime in LHCII ($\tau_D$ ∼1.2 ns), indicating that singlet excitons in LHCII are diffusion-limited.

# Discussion

Our findings revealed long-range exciton diffusion in LHCII with a diffusivity of $3 \times 10^{-2}$ $\mu m^2 ns^{-1}$. With this characteristic diffusion length, exciton transport extends hundreds of nanometers across light-harvesting antenna complexes, likely key to the high efficiency even with the large supercomplexes of 20 to 30 nm observed in some photosynthetic organisms.[38,47] In the

biomolecular films, the impressive diffusivity plays a pivotal role in enabling LHCII to deliver excitons to RC-LH1, as it ensures that additional excitons from the LHCII only region reach the overlap region for subsequent transfer to the acceptor and charge separation.[19] Moreover, our simulations revealed anisotropic exciton diffusion, with preferential transport along the LHCII linear pattern and reduced diffusion in the orthogonal direction. This anisotropy likely arises from excitonic confinement in the transverse direction, guiding excitons toward the overlap region where energy transfer to RC-LH1 occurs. Similar directional energy guiding occurs in LH2 arrays,[38] and our results suggest that LHCII exhibits comparable behavior, despite the reduced dimensional confinement in our system. The directional guiding even with moderate confinement demonstrates that such architectures offer a robust pathway to optimize nanoscale platforms for optoelectronic applications.

The long-range exciton diffusion combined with the 30% energy transfer efficiency enhances the capacity and effective absorption cross-section of the solar energy conversion machinery (RC-LH1). Such enhancement is particularly crucial under natural conditions where sunlight is a dilute energy source, with only one photon per chlorophyll per second.[48] Thus, the sensitization of RC-LH1 by LHCII provides a significant boost to the performance in solar energy conversion. To characterize the performance of our nanoscale platform, we can estimate the solar energy conversion efficiency within the overlap regions upon LHCII excitation. In these regions, a 30% energy transfer efficiency ($\eta_{ETE}$) was observed in our LHCII/RC-LH1 network, even in the context of the large spectral separation between the proteins. By evaluating the quantum efficiency ($\eta_{QE} = \eta_{ETE} * \eta_{CSE}$) of our system, and considering that the charge separation efficiency of RC-LH1 ($\eta_{CSE}$) is nearly 100% in purple bacteria, we determined that ($\eta_Q$) is around 30% in the overlap regions, although it decreases to $\sim$5% for the entire platform when considering the large LHCII only regions in the current architecture. The 30% efficiency is notable when compared to solar cells, where even the most advanced single-junction solar cells can only reach the Shockley–Queisser limit of

33%, and state-of-the-art silicon-based multi-junction solar cells achieve a maximum yield of 40%.[49] However, differences in the absorption spectra, the conversion mechanism, and the charge extraction process make direct comparisons between biological and photovoltaic systems complex.

Overall, high energy transfer efficiency between LHCII and RC-LH1 is achieved despite their spectral separation. The high efficiency, combined with the long exciton diffusion length in protein networks, enhances the overall performance. Our results suggest that designing protein networks with long-range exciton diffusion, even with non-native protein combinations, provides an effective strategy for expanding the spectral range of solar energy capture. By harnessing exciton diffusion and optimizing energy transport across protein networks, we created an efficient nanoscale platform capable of capturing and converting a broad spectrum of solar energy, emphasizing the potential for integrating light-harvesting proteins from different photosynthetic species.

## Conclusion

In conclusion, this study provides new insights into the spatial and diffusion dynamics of excitons within light-harvesting complexes LHCII and RC-LH1, quantifying and emphasizing the significant role of exciton diffusion in facilitating energy transfer. By analyzing intensity profiles at the edges and overlap regions, we demonstrated that the characteristic broadening observed in LHCII arises from long-range exciton diffusion, as supported by spatiotemporal simulations. Our simulations, validated against experimental data, show that LHCII exhibits a diffusivity of $3 \times 10^{-2}\,\mu m^2 ns^{-1}$ and anisotropic exciton diffusion likely due to structural confinement within the transverse direction.

This directional exciton behavior points to the broader applicability of controlled diffusion

mechanisms in optimizing energy transfer efficiencies in artificial photosynthetic systems and nanostructured biohybrid devices. The refined parameters derived from our simulations offer a quantitative framework for predicting and tailoring exciton behavior in biomolecular films. These findings contribute to a deeper understanding of exciton diffusion properties in complex protein networks and underscore the potential of using targeted architectures to advance sustainable energy technologies. Such a design could therefore be applied to existing artificial biophotovoltaic devices to further improve their energy capture efficiency.[13]

# Methods

## Sample fabrication

LHCII was purified from dark-adapted spinach leaves as described previously.[50] RC-LH1 was purified from semi-aerobically grown cells of *Rba. sphaeroides* cells were harvested and disrupted using a French press at 18,000 psi. After centrifugation, the supernatant was loaded onto a 15/40% (w/w) sucrose gradient that was centrifuged at 50,000 g for 5 hours to isolate the intracytoplasmic membranes (ICM). After harvesting, the ICMs were solubilized in 3% (v/v) $\beta$-DDM by stirring in the dark at 4 °C for 45 min. The solubilized membrane solution was diluted at least three-fold in 10 mM HEPES pH 7.8, 50 mM NaCl, 0.03% (v/v) $\beta$-DDM and centrifuged for 1 hour at 160,000g (4 °C) to remove unsolubilized material. RC-LH1 was purified using a DEAE ion-exchange column eluted with a 50-300 mM NaCl gradient, followed by gel filtration on a Cytiva HiLoad 16/600 Superdex 200 pg column in 10 mM HEPES pH 7.8, 50mM NaCl, 0.03% (v/v) $\beta$-DDM. Fractions with a A870/A280 absorbance ratio greater than 1.9 were pooled, concentrated and flash frozen in liquid nitrogen before storing at −70 °C. The soft-patterning was performed using PDMS stamps prepared as per *Huang et al.*[10] on glass coverslips (German Glass Cover Slips, #1.5, 25 mm dia.). The PDMS stamp was covered with 20 $\mu$M LHCII or RC-LH1 solution for 10 mins, then blown dry with nitrogen to form a surface layer of protein. The LHCII inked stamp was gently

placed onto the coverslip to print an array and left for 10 mins before being gently lifted away. RC-LH1 was printed at a roughly 90-degree orientation to the previous LHCII arrays to form the cross-pattern. The Si master template (Mikromasch, TGZ11) with linear arrays of 5 µm width, 10 µm pitch, and 1.35 µm step height was used as master to replicate a polydimethylsiloxane (PDMS) stamp. Prior to casting the PDMS mixture, the Si master template was treated in trichlorosilane (Sigma-Aldrich) vapor under a vacuum (20 mbar) for 16 hours. The PDMS mixture was prepared by mixing Sylgard184 silicon elastomer base (Dow Corning) and Sylgard184 silicon elastomer curing agent (Dow Corning) at a ratio of 10:1. The PDMS mixture was stirred for five minutes to reach uniformity and centrifuged at 3000 × g for 15 min to remove air bubbles. Then the PDMS mixture was cast onto the Si master and cured at 74 °C for 8 h, before being carefully detached as a PDMS replica stamp.

## AFM characterisation

AFM data was collected on a Multimode 8 instrument equipped with a 15 µm scanner (E-scanner) coupled to a NanoScope V controller (Bruker). The patterned surfaces were imaged in PeakForce Tapping mode, in the air at room temperature using Bruker SNL-10 probes (23 kHz, k ∼0.12 $\mathrm{Nm}^{-1}$). The images were taken using 256 x 265 pixel arrays at a scan rate between 1-2 Hz.

## Optical characterisation

Spatially-resolved fluorescence emission was recorded using a home-built inverted confocal microscope. The sample was excited using a pulsed source centered at 630 nm with a peak excitation fluence of 0.5 µJ$\mathrm{cm}^{-2}$. A mode-locked Ti:sapphire laser (Vitara, Coherent), emitting 15 fs pulses at 800 nm with a repetition rate of 80 MHz, was used to pump a nonlinear photonic crystal fiber (FemtoWhite 800, Newport), generating a supercontinuum light. The pulse length was stretched to approximately 10 ps by propagation through a 16 m optical single-mode fiber (PM-S405-XP, Thorlabs). The desired wavelength window was selected by

spectral filtering (ET645/30x, Chroma). The excitation wavelength (∼630 nm) was chosen to predominantly excite LHCII, facilitating the study of energy transfer from LHCII to RC-LH1 (see Figure 1b), although RC-LH1 also absorbs a small portion ( 10%) of the excitation.

The excitation beam was then injected into an inverted microscope (RM21-AZ-AXY, Mad City Labs) and focused onto the sample using a silicon oil immersion objective (UPLSAPO100XO, NA 1.4, Olympus), yielding an excitation spot with a full-width half-maximum (FWHM) of approximately 225 nm (see Figure 1a). Fluorescence emitted from the sample was collected through the same objective and separated from the excitation path by a dichroic mirror (FF01-629/56-25, Semrock). To reject out-of-focus background fluorescence, a confocal filter was employed, consisting of two 150 mm focal length achromatic doublet lenses (AC254-150-A, Thorlabs) and a 50 µm pinhole.

The fluorescence signals from LHCII and RC-LH1, at 700 nm and 900 nm, respectively (see Figure 1b), were separated by a dichroic mirror (FF01-834/LP-25, Semrock), spectrally filtered (LHCII: ET700/75m, Chroma; RC-LH1: FF01-834/LP-25, Semrock), and detected separately by two APDs (SPCM-AQRH, Excelitas). Fluorescence decays were measured by connecting the two APDs to a time-correlated single-photon counting (TCSPC) module (PicoHarp 300/800, PicoQuant). The instrument response function (IRF) width of the APDs, measured from the excitation scattering on a glass coverslip, was 120 ps. The signal was then scanned across the sample using high-precision piezoelectric scanners (Nano-LP/Nano-Drive, Mad City Labs) with a scanning range of 100x100x200 µm.

## Data acquisition and analysis

The entire setup was controlled using the open-source Qudi Python software suite,[51] enabling the simultaneous recording of the time-dependant fluorescence of LHCII and RC-LH1 at each point of the scanned areas. Fluorescence lifetime images (FLIM) were obtained post-

acquisition using an automatic fitting procedure implemented in a custom Python script. Fluorescence lifetime fitting was performed by convolving the IRF with a mono-exponential decay.

# References


(1) Baghbanzadeh, S.; Kassal, I. Geometry, Supertransfer, and Optimality in the Light Harvesting of Purple Bacteria. *The Journal of Physical Chemistry Letters* **2016**, *7*, 3804–3811, Publisher: American Chemical Society.

(2) Wraight, C. A.; Clayton, R. K. The absolute quantum efficiency of bacteriochlorophyll photooxidation in reaction centres of Rhodopseudomonas spheroides. *Biochimica Et Biophysica Acta* **1974**, *333*, 246–260.

(3) Skillman, J. B. Quantum yield variation across the three pathways of photosynthesis: not yet out of the dark. *Journal of Experimental Botany* **2008**, *59*, 1647–1661.

(4) Timpmann, K.; Chenchiliyan, M.; Jalviste, E.; Timney, J. A.; Hunter, C. N.; Freiberg, A. Efficiency of light harvesting in a photosynthetic bacterium adapted to different levels of light. *Biochimica et Biophysica Acta (BBA) - Bioenergetics* **2014**, *1837*, 1835–1846.

(5) Proppe, A. H. et al. Bioinspiration in light harvesting and catalysis. *Nature Reviews Materials* **2020**, *5*, 828–846, Publisher: Nature Publishing Group.

(6) Vasilev, C.; Johnson, M. P.; Gonzales, E.; Wang, L.; Ruban, A. V.; Montano, G.; Cadby, A. J.; Hunter, C. N. Reversible Switching between Nonquenched and Quenched States in Nanoscale Linear Arrays of Plant Light-Harvesting Antenna Complexes. *Langmuir* **2014**, *30*, 8481–8490.

(7) Patole, S.; Vasilev, C.; El-Zubir, O.; Wang, L.; Johnson, M. P.; Cadby, A. J.;

Leggett, G. J.; Hunter, C. N. Interference lithographic nanopatterning of plant and bacterial light-harvesting complexes on gold substrates. *Interface Focus* **2015**, *5*, 20150005.

(8) Lishchuk, A.; Kodali, G.; Mancini, J. A.; Broadbent, M.; Darroch, B.; Mass, O. A.; Nabok, A.; Dutton, P. L.; Hunter, C. N.; Törmä, P.; Leggett, G. J. A synthetic biological quantum optical system †Electronic supplementary information (ESI) available: Full details of all of the experimental materials and methods, together with detailed surface characterisation data obtained using X-ray photoelectron spectroscopy and spectroscopic ellipsometry. See DOI: 10.1039/c8nr02144a. *Nanoscale* **2018**, *10*, 13064–13073.

(9) Lishchuk, A.; Vasilev, C.; Johnson, M. P.; Hunter, C. N.; Törmä, P.; Leggett, G. J. Turning the challenge of quantum biology on its head: biological control of quantum optical systems. *Faraday Discussions* **2019**, *216*, 57–71, Publisher: The Royal Society of Chemistry.

(10) Huang, X.; Vasilev, C.; Hunter, C. N. Excitation energy transfer between monomolecular layers of light harvesting LH2 and LH1-reaction centre complexes printed on a glass substrate. *Lab on a Chip* **2020**, *20*, 2529–2538.

(11) Huang, X.; Hunter, C. N.; Vasilev, C. Multicomponent Nanoscale Patterning of Functional Light-Harvesting Protein Complexes by Local Oxidation Lithography. *Advanced Materials Interfaces* **2021**, *8*, 2001670.

(12) Ennist, N. M. et al. De novo design of proteins housing excitonically coupled chlorophyll special pairs. *Nature Chemical Biology* **2024**, *20*, 906–915.

(13) Qiu, X.; Castañeda Ocampo, O.; de Vries, H. W.; van Putten, M.; Loznik, M.; Hermann, A.; Chiechi, R. C. Self-Regenerating Soft Biophotovoltaic Devices. *ACS Applied Materials & Interfaces* **2018**, *10*, 37625–37633, Publisher: American Chemical Society.

(14) Roberts, D. T.; Sadeghi, S. M. Excitation-Dependent Exciton Diffusion in Semicon-

ductor Quantum Dot Thin Films with Spatially Patterned Lifetimes. *ACS Photonics* **2024**, *11*, 2578–2586.

(15) Lo Gerfo M., G.; Bolzonello, L.; Bernal-Texca, F.; Martorell, J.; Van Hulst, N. F. Spatiotemporal Mapping Uncouples Exciton Diffusion from Singlet–Singlet Annihilation in the Electron Acceptor Y6. *The Journal of Physical Chemistry Letters* **2023**, *14*, 1999–2005.

(16) Chandrabose, S.; Chen, K.; Barker, A. J.; Sutton, J. J.; Prasad, S. K. K.; Zhu, J.; Zhou, J.; Gordon, K. C.; Xie, Z.; Zhan, X.; Hodgkiss, J. M. High Exciton Diffusion Coefficients in Fused Ring Electron Acceptor Films. *Journal of the American Chemical Society* **2019**, *141*, 6922–6929.

(17) Firdaus, Y. et al. Long-range exciton diffusion in molecular non-fullerene acceptors. *Nature Communications* **2020**, *11*, 5220.

(18) Rai, D.; Holmes, R. J. Measurement of the triplet exciton diffusion length in organic semiconductors. *Journal of Materials Chemistry C* **2019**, *7*, 5695–5701, Publisher: The Royal Society of Chemistry.

(19) Sajjad, M. T.; Ruseckas, A.; Samuel, I. D. W. Enhancing Exciton Diffusion Length Provides New Opportunities for Organic Photovoltaics. *Matter* **2020**, *3*, 341–354.

(20) Croce, R.; Carmo-Silva, E.; Cho, Y. B.; Ermakova, M.; Harbinson, J.; Lawson, T.; McCormick, A. J.; Niyogi, K. K.; Ort, D. R.; Patel-Tupper, D.; Pesaresi, P.; Raines, C.; Weber, A. P. M.; Zhu, X.-G. Perspectives on improving photosynthesis to increase crop yield. *The Plant Cell* **2024**, *36*, 3944–3973.

(21) Ballottari, M.; Girardon, J.; Dall'Osto, L.; Bassi, R. Evolution and functional properties of Photosystem II light harvesting complexes in eukaryotes. *Biochimica et Biophysica Acta (BBA) - Bioenergetics* **2012**, *1817*, 143–157.

(22) Fleming, G. R.; Schlau-Cohen, G. S.; Amarnath, K.; Zaks, J. Design principles of photosynthetic light-harvesting. *Faraday Discussions* **2012**, *155*, 27–41, Publisher: The Royal Society of Chemistry.

(23) Swainsbury, D. J.; Faries, K. M.; Niedzwiedzki, D. M.; Martin, E. C.; Flinders, A. J.; Canniffe, D. P.; Shen, G.; Bryant, D. A.; Kirmaier, C.; Holten, D.; Hunter, C. N. Engineering of B800 bacteriochlorophyll binding site specificity in the Rhodobacter sphaeroides LH2 antenna. *Biochimica et Biophysica Acta (BBA) - Bioenergetics* **2019**, *1860*, 209–223.

(24) Almosni, S. et al. Material challenges for solar cells in the twenty-first century: directions in emerging technologies. *Science and Technology of Advanced Materials* **2018**, *19*, 336–369.

(25) Liu, J.; Friebe, V. M.; Frese, R. N.; Jones, M. R. Polychromatic solar energy conversion in pigment-protein chimeras that unite the two kingdoms of (bacterio)chlorophyll-based photosynthesis. *Nature Communications* **2020**, *11*, 1542.

(26) Caffarri, S.; Croce, R.; Breton, J.; Bassi, R. The Major Antenna Complex of Photosystem II Has a Xanthophyll Binding Site Not Involved in Light Harvesting*. *Journal of Biological Chemistry* **2001**, *276*, 35924–35933.

(27) Qian, P.; Addlesee, H. A.; Ruban, A. V.; Wang, P.; Bullough, P. A.; Hunter, C. N. A Reaction Center-Light-harvesting 1 Complex (RC-LH1) from a *Rhodospirillum rubrum* Mutant with Altered Esterifying Pigments. *Journal of Biological Chemistry* **2003**, *278*, 23678–23685.

(28) Razjivin, A.; Solov'ev, A.; Kompanets, V.; Chekalin, S.; Moskalenko, A.; Lokstein, H. The origin of the "dark" absorption band near 675 nm in the purple bacterial core light-harvesting complex LH1: two-photon measurements of LH1 and its subunit B820. *Photosynthesis Research* **2019**, *140*, 207–213.

(29) Drop, B.; Webber-Birungi, M.; Yadav, S. K. N.; Filipowicz-Szymanska, A.; Fusetti, F.; Boekema, E. J.; Croce, R. Light-harvesting complex II (LHCII) and its supramolecular organization in *Chlamydomonas reinhardtii*. *Biochimica et Biophysica Acta (BBA) - Bioenergetics* **2014**, *1837*, 63–72.

(30) Adams, P. G.; Vasilev, C.; Hunter, C. N.; Johnson, M. P. Correlated fluorescence quenching and topographic mapping of Light-Harvesting Complex II within surface-assembled aggregates and lipid bilayers. *Biochimica et Biophysica Acta (BBA) - Bioenergetics* **2018**, *1859*, 1075–1085.

(31) Iwai, M.; Chen, J.-J.; Park, S.; Yoneda, Y.; Schmid, E. M.; Fletcher, D. A.; Fleming, G. R.; Niyogi, K. K. Variable optical properties of light-harvesting complex II revisited. 2020; `https://www.biorxiv.org/content/10.1101/2020.10.05.312405v1`, Pages: 2020.10.05.312405 Section: New Results.

(32) Moya, I.; Silvestri, M.; Vallon, O.; Cinque, G.; Bassi, R. Time-Resolved Fluorescence Analysis of the Photosystem II Antenna Proteins in Detergent Micelles and Liposomes. *Biochemistry* **2001**, *40*, 12552–12561.

(33) Ruban, A. V.; Young, A.; Horton, P. Modulation of chlorophyll fluorescence quenching in isolated light harvesting complex of Photosystem II. *Biochimica et Biophysica Acta (BBA) - Bioenergetics* **1994**, *1186*, 123–127.

(34) Son, M.; Moya, R.; Pinnola, A.; Bassi, R.; Schlau-Cohen, G. S. Protein–Protein Interactions Induce pH-Dependent and Zeaxanthin-Independent Photoprotection in the Plant Light-Harvesting Complex, LHCII. *Journal of the American Chemical Society* **2021**, *143*, 17577–17586, Publisher: American Chemical Society.

(35) Scholes, G. D. Long-Range Resonance Energy Transfer in Molecular Systems. *Annual Review of Physical Chemistry* **2003**, *54*, 57–87, Publisher: Annual Reviews.

(36) Gopich, I. V.; Szabo, A. Theory of the energy transfer efficiency and fluorescence lifetime distribution in single-molecule FRET. *Proceedings of the National Academy of Sciences* **2012**, *109*, 7747–7752.

(37) Seitz, M.; Magdaleno, A. J.; Alcázar-Cano, N.; Meléndez, M.; Lubbers, T. J.; Walraven, S. W.; Pakdel, S.; Prada, E.; Delgado-Buscalioni, R.; Prins, F. Exciton diffusion in two-dimensional metal-halide perovskites. *Nature Communications* **2020**, *11*, 2035, Publisher: Nature Publishing Group.

(38) Escalante, M.; Lenferink, A.; Zhao, Y.; Tas, N.; Huskens, J.; Hunter, C. N.; Subramaniam, V.; Otto, C. Long-Range Energy Propagation in Nanometer Arrays of Light Harvesting Antenna Complexes. *Nano Letters* **2010**, *10*, 1450–1457, Publisher: American Chemical Society.

(39) Bennett, D. I. G.; Amarnath, K.; Fleming, G. R. A Structure-Based Model of Energy Transfer Reveals the Principles of Light Harvesting in Photosystem II Supercomplexes. *Journal of the American Chemical Society* **2013**, *135*, 9164–9173, Publisher: American Chemical Society.

(40) Ruan, M.; Li, H.; Zhang, Y.; Zhao, R.; Zhang, J.; Wang, Y.; Gao, J.; Wang, Z.; Wang, Y.; Sun, D.; Ding, W.; Weng, Y. Cryo-EM structures of LHCII in photo-active and photo-protecting states reveal allosteric regulation of light harvesting and excess energy dissipation. *Nature Plants* **2023**, *9*, 1547–1557, Publisher: Nature Publishing Group.

(41) Schlau-Cohen, G. S.; Calhoun, T. R.; Ginsberg, N. S.; Read, E. L.; Ballottari, M.; Bassi, R.; van Grondelle, R.; Fleming, G. R. Pathways of Energy Flow in LHCII from Two-Dimensional Electronic Spectroscopy. *The Journal of Physical Chemistry B* **2009**, *113*, 15352–15363, Publisher: American Chemical Society.

(42) Amarnath, K.; Bennett, D. I. G.; Schneider, A. R.; Fleming, G. R. Multiscale model

of light harvesting by photosystem II in plants. *Proceedings of the National Academy of Sciences* **2016**, *113*, 1156–1161, Publisher: Proceedings of the National Academy of Sciences.

(43) Lee, T.-Y.; Lam, L.; Patel-Tupper, D.; Roy, P. P.; Ma, S. A.; Lam, H. E.; Lucas-DeMott, A.; Karavolias, N. G.; Iwai, M.; Niyogi, K. K.; Fleming, G. R. Chlorophyll to zeaxanthin energy transfer in nonphotochemical quenching: An exciton annihilation-free transient absorption study. *Proceedings of the National Academy of Sciences* **2024**, *121*, e2411620121.

(44) Brinatti Vazquez, G. D.; Lo Gerfo Morganti, G.; Vasilev, C.; Hunter, C. N.; Van Hulst, N. F. Structured Excitation Energy Transfer: Tracking Exciton Diffusion below Sunlight Intensity. *ACS Photonics* **2024**, *11*, 1318–1326.

(45) Swenberg, C. E.; Geacintov, N. E.; Breton, J. Laser Pulse Excitation Studies of the Fluorescence of Chloroplasts. *Photochemistry and Photobiology* **1978**, *28*, 999–1006, _eprint: https://onlinelibrary.wiley.com/doi/pdf/10.1111/j.1751-1097.1978.tb07738.x.

(46) Michael Gruber, J.; Chmeliov, J.; Krüger, T. P. J.; Valkunas, L.; Van Grondelle, R. Singlet–triplet annihilation in single LHCII complexes. *Physical Chemistry Chemical Physics* **2015**, *17*, 19844–19853.

(47) Qian, P.; Neil Hunter, C.; Bullough, P. A. The 8.5Å Projection Structure of the Core RC–LH1–PufX Dimer of Rhodobacter sphaeroides. *Journal of Molecular Biology* **2005**, *349*, 948–960.

(48) Blankenship, R. E. et al. Comparing photosynthetic and photovoltaic efficiencies and recognizing the potential for improvement. *Science (New York, N.Y.)* **2011**, *332*, 805–809.

(49) Best Research-Cell Efficiency Chart. `https://www.nrel.gov/pv/cell-efficiency.html`.

(50) Manna, P.; Davies, T.; Hoffmann, M.; Johnson, M. P.; Schlau-Cohen, G. S. Membrane-dependent heterogeneity of LHCII characterized using single-molecule spectroscopy. *Biophysical Journal* **2021**, *120*, 3091–3102.

(51) Binder, J. M.; Stark, A.; Tomek, N.; Scheuer, J.; Frank, F.; Jahnke, K. D.; Müller, C.; Schmitt, S.; Metsch, M. H.; Unden, T.; Gehring, T.; Huck, A.; Andersen, U. L.; Rogers, L. J.; Jelezko, F. Qudi: A modular python suite for experiment control and data processing. *SoftwareX* **2017**, *6*, 85–90.

# Supporting Information

## AFM analysis summary of our protein network

Table S0: Extracted heights and root mean-squared deviation (RMSD) of the AFM profiles showed in Figure 1d.

| | LHCII only | RC-LH1 only | LHCII overlap | RC-LH1 overlap |
|---|---|---|---|---|
| Heights | $5.0 \pm 0.7\,\text{nm}$ | $14.0 \pm 0.5\,\text{nm}$ | $19.0 \pm 0.8\,\text{nm}$ | $19.0 \pm 1.1\,\text{nm}$ |
| RMSD | $1.7 \pm 0.5\,\text{nm}$ | $0.7 \pm 0.3\,\text{nm}$ | $1.5 \pm 0.7\,\text{nm}$ | $1.4 \pm 0.8\,\text{nm}$ |

## Exciton diffusion FDTD simulations

Numerical simulations of exciton diffusion were derived from Equations 5 and 6 using the finite-difference time-domain (FDTD) formalism. This method discretizes both space and time to solve the diffusion equations for exciton populations in a 2D network. The governing equations are:

$$n_D^{i,j;k+1} = n_D^{i,j;k} + \frac{\delta t}{\delta l^2}\left[D_x\left(n_D^{i+1,j;k} + n_D^{i-1,j;k} - 2n_D^{i,j;k}\right) + D_y\left(n_D^{i,j+1;k} + n_D^{i,j-1;k} - 2n_D^{i,j;k}\right)\right] - \delta t\left(k_D + k_{ET}\right) n_D^{i,j;k} \tag{1}$$

$$n_A^{i,j;k+1} = n_A^{i,j;k} + \delta t\left(k_{ET} n_D^{i,j;k} - k_A n_A^{i,j;k}\right) \tag{2}$$

Here, $n_D^{i,j;k} = n_D(x_i, y_j; t_k)$ and $n_A^{i,j;k} = n_A(x_i, y_j; t_k)$ represent the exciton densities of the donor (LHCII) and acceptor (RC-LH1) on a 63x63 grid at time $t_k = k \cdot \delta t$, with $\delta t = 0.1\,\text{ns}$. The spatial coordinates are given by $x_i = i \cdot \delta l$ and $y_j = j \cdot \delta l$, with $\delta l = 150\,\text{nm}$, using an isotropic space such that $\delta x = \delta y = \delta l$.

The LHCII and RC-LH1 patterns were defined using binary masks, $\chi_D$ and $\chi_A$, respectively. These masks have 5 µm strips centered in the middle of each mask, representing the

regions where donors and acceptors are present. The masks constrain exciton diffusion within the LHCII pattern by modifying the diffusion coefficients $D'_{x,y} = D_{x,y}\chi_D$, and they limit energy transfer to the overlap region by adjusting the energy transfer rate $k'_{ET} = k_{ET}\chi_D\chi_A$.

The simulations were initialized with the donor population $n_D(x_i, y_j, 0) = \chi_D$ and the acceptor population $n_A(x_i, y_j, 0) = 0.1\chi_A$, where the factor of 0.1 for $n_A$ represents a 10% absorption ratio relative to $n_D$ (as shown in Figure 1b). The exciton populations were then iteratively updated using the FDTD method, with each time step $t_{k+1}$ computed from the previous step $t_k$.

To reproduce our confocal measurements, we excited only one pixel at a time and systematically ran simulations for each iteration. These simulations were then averaged to represent the measured fluorescence intensity. Finally, we applied a 150 nm Gaussian filter to the resulting images to account for the diffraction limit of our microscope.

The parameters $k_D$, $k_A$, and $k_{ET}$ were derived from FLIM (Fluorescence Lifetime Imaging Microscopy) measurements, while the diffusion coefficients $D_x$ and $D_y$ were treated as free parameters. The best-fit parameters, yielding the closest match to experimental data, are listed in Table 1. The resulting intensity maps, integrated over time, and FLIM maps are shown in Figure S1.

These simulations provide insights into the exciton diffusion and energy transfer processes in a 2D network, mimicking the behavior observed in confocal measurements. The simulated intensity profiles, extracted from the simulation, are shown as solid lines in Figure 3b-e and are compared with experimental data.

To study the robustness of our model, we repeated the simulations at different spatial steps (70 nm, 120 nm, and 150 nm). We obtained very similar values, within error bars, for the width of the fitted profiles, thus demonstrating the robustness of our model.

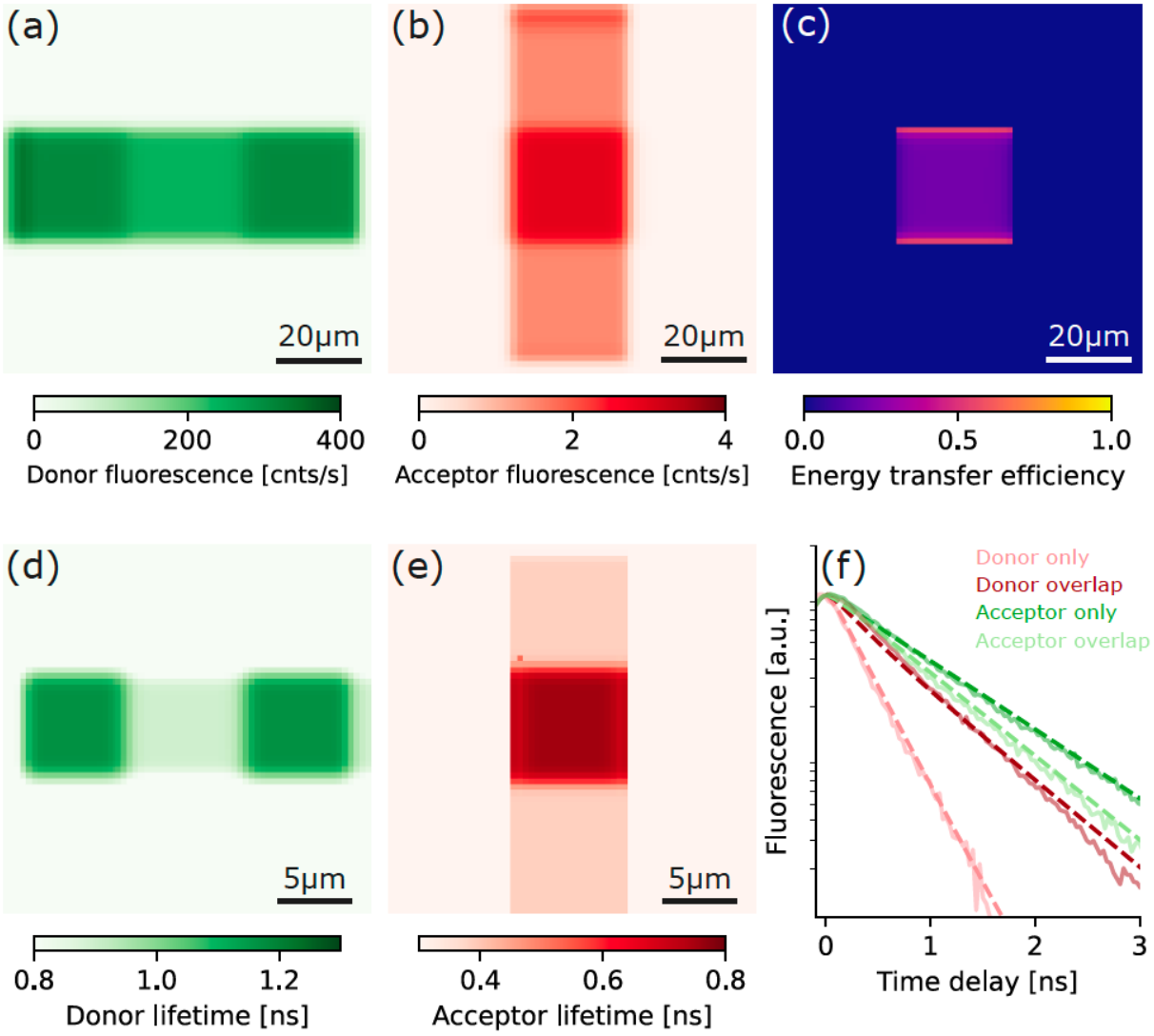


Figure S1: Maps of the donor and acceptor population density (a, b) and lifetime (d, e) resulting from our FDTD simulations. (c) Energy transfer efficiency map derived from the donor population density in panel (a). (f) Time decay of the donor (green solid lines) and acceptor (red solid lines) populations, with darker (lighter) lines taken inside (outside) the overlap regions.

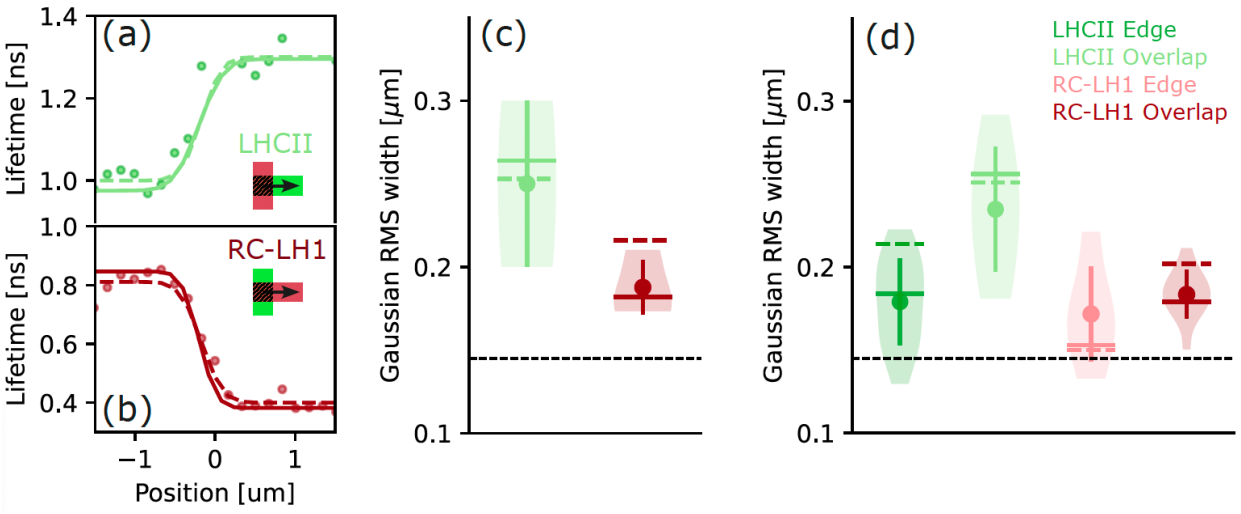


Figure S2: (a, b) Spatial variation of the fluorescence lifetime for RC-LH1 (a) and LHCII (b) across the overlap regions, extracted from Figure 2. Experimental data points are shown with fitted curves as dashed lines, and simulated profiles are represented by solid lines. (c, d) Root-mean-squared (RMS) widths extracted from the lifetime (c) and intensity (d) profiles. The violin plots depict the distributions of experimental values, with mean values and standard deviations shown as points and error bars. Dashed and solid horizontal lines in (c) and (d) correspond to RMS widths derived from FDTD simulations, representing isotropic diffusion (Dx = Dy) and anisotropic diffusion (Dx = 0.4Dy), respectively.

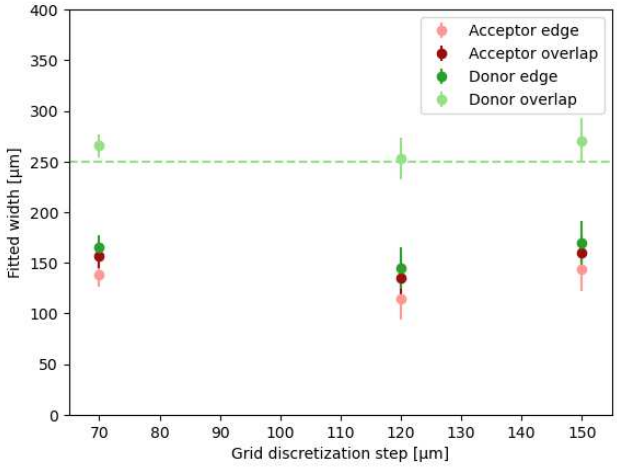


Figure S3: Results of the simulation of the exciton diffusion in the protein network presenting the fitted width, shown with errorbars, of the simulated intensity profiles for three different step sizes: 70 nm, 120 nm, and 150 nm.

## Power-dependent study

The fluorescence intensity and lifetime were analyzed as a function of excitation fluence, extracted from the fluorescence map of the same area for both LHCII (red points) and RC-LH1 (green points), inside (darker points) and outside (lighter points) the overlap regions. The results of this power-dependent study are shown in Figure S4. The intensity and lifetime values were extracted from each region using masks, and the error bars reflect the spatial variation in intensity and lifetime across the region.

To model our power-dependent data, we applied the following singlet-triplet annihilation model:[46]

$$\frac{dn_D}{dt} = G(t) - (k_D + k_{ET} + k_{ISC})n_D - \gamma_{st}^D n_D n_D^t \tag{3}$$

$$\frac{dn_A}{dt} = k_{ET} n_D(t) - (k_A + k_{ISC})n_A - \gamma_{st}^A n_A n_A^t \tag{4}$$

$$\frac{dn_D^t}{dt} = k_{ISC} n_D - K_t n_D^t \tag{5}$$

$$\frac{dn_A^t}{dt} = k_{ISC} n_A - K_t n_A^t \tag{6}$$

where $n_D^t$ and $n_A^t$ represent the triplet exciton populations, $k_{ISC}$ is the inter-system crossing rate, $\gamma_{st}^D$ and $\gamma_{st}^A$ are the donor and acceptor singlet-triplet annihilation rates, and $K_t$ is the triplet recombination rate. The remaining parameters are as previously defined, and we used the same values (see Table 1), with the exception of $k_{ET} \approx 0.3\,\mathrm{ns}^{-1}$. The lower value of $k_{ET}$ can be explained by a reduction in energy transfer efficiency due to repeated scans at increasing power. We assume that both donor and acceptor share the same values for $k_{ISC}$ and $K_t$, as triplet excitons in chlorophyll are weakly sensitive to their environment due to

their low oscillator strength. As in the previous section, the generation term was replaced by initial populations, and the initial excitation of each population per $\mathrm{Wcm}^{-2}$ excitation fluence is summarized in Table S3.

Table S3: Values of the parameters used for the singlet-triplet annihilation model.

| Parameters | $K_t$ | $k_{ISC}$ | $\gamma_{st}^D$ | $\gamma_{st}^A$ | $n_D(0)$, $n_A(0)$, $n_D^t(0)$, $n_A^t(0)$ |
|---|---|---|---|---|---|
| Values | $1/7000\,\mathrm{ns}^{-1}$ | $1/8.54\,\mathrm{ns}^{-1}$ | $0.7\,\mathrm{ns}^{-1}$ | $0.03\,\mathrm{ns}^{-1}$ | 0.015, 0.006, 0.0003, $0/\mathrm{Wcm}^{-2}$ |

To model our data, we solved these ordinary differential equations (ODEs) for various excitation fluences and fit the population decays using a mono-exponential function. We used values similar to those reported by *Gruber et al.*, with minor adaptations for the initial excitation (which was multiplied by 200 to account for the approximate number of LHCII molecules under our excitation spot) and the singlet-triplet annihilation rates. The results of the numerical model, shown as dashed lines in Figure S4, successfully reproduce the experimental data, allowing us to attribute this power dependence to singlet-triplet annihilation. From the value of $\gamma_{st}^D$, we estimate a singlet exciton diffusion length of approximately 200 nm, using the relation $L_D = \sqrt{\frac{\gamma_{st}^D \tau_D}{\pi R^2}}$, with $R \approx 140\,\mathrm{nm}$ as the excitation radius.

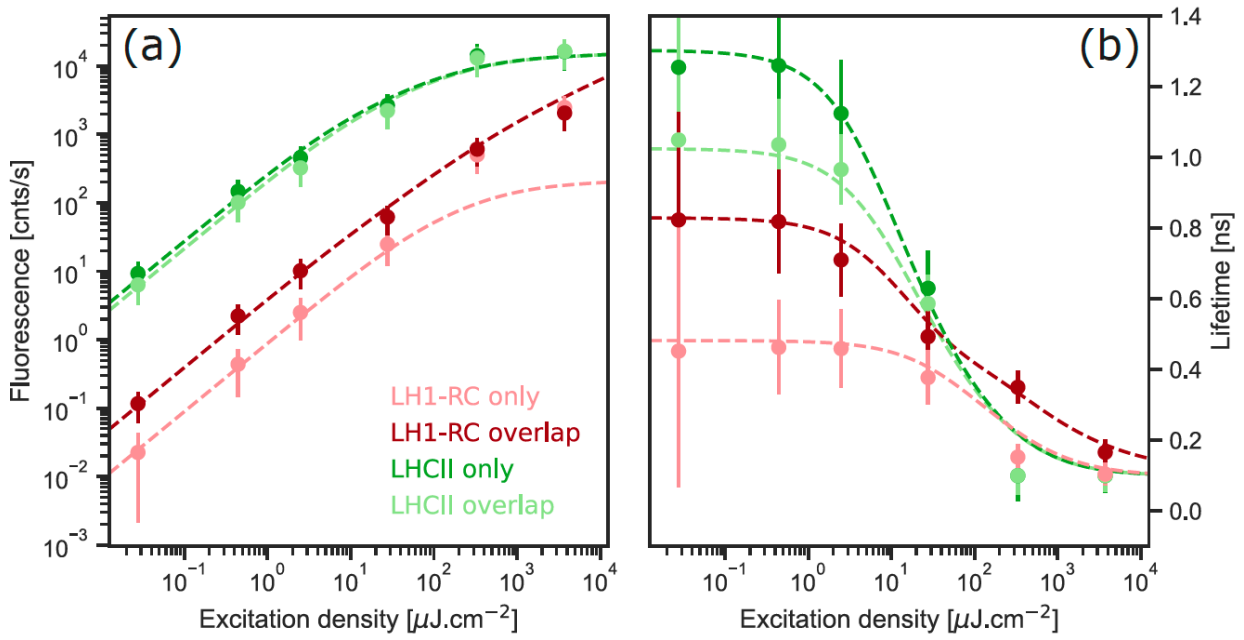


Figure S4: Fluorescence intensity (a) and lifetime (b) of donor (red dots) and acceptor (green dots) channels inside (darker dots) and outside (lighter dots) the overlap regions. The dashed lines represent the results obtained from the singlet-triplet annihilation (STA) rate equations.